

Aqueous Conversion of Fructose Phosphate Precursor Nanoparticles into Emissive C-Dot Composite Nanoparticles

Kristina Sabljo,^[a] Radian Popescu,^[b] Nadine C. Michenfelder,^[c] Andreas-Neil Unterreiner,^[c] Dagmar Gerthsen,^[b] and Claus Feldmann*^[a]

Abstract: A one-pot, fully water-based synthesis of blue- and red-emitting C-dots is presented. To this concern, $[\text{ZrO}]^{2+}$ $[\text{F6P}]^{2-}$ and $[\text{Eu}(\text{OH})]^{2+}$ $[\text{F6P}]^{2-}$ precursor nanoparticles (F6P: D-fructose-6-phosphate) are prepared in water and converted to C-dot@ $[\text{ZrO}]^{2+}$ $[\text{HPO}_4]^{2-}$ and C-dot@ $[\text{Eu}(\text{OH})]^{2+}$ $[\text{HPO}_4]^{2-}$ composite nanoparticles in boiling water (100 °C) via microwave heating. Composition, structure, and fluorescence of the composite nanoparticles are validated by different

analytical methods (e.g., FT-IR, EA, TG, DLS, SEM, TEM, EDXS). The resulting aqueous suspensions are characterized by high colloidal stability and intense emission. Specifically, C-dot@ $[\text{Eu}(\text{OH})]^{2+}$ $[\text{HPO}_4]^{2-}$ exhibits Eu^{3+} -type red emission in water. The one-pot water-based synthesis with fructose-containing precursor nanoparticles and the structure of the phosphate-stabilized C-dot composite nanoparticles are reported for the first time.

1. Introduction

Carbon dots (C-dots) represent a unique type of carbon modification that contrasts with diamond, graphite, fullerenes, graphene, carbon nanotubes, and carbyne.^[1] Since their discovery in 2004,^[2] their synthesis, structure, and properties have been intensely studied.^[3] C-dots combine attractive properties such as high stability, low cost, low toxicity, adaptable surface functionalization, or good conductivity. The most outstanding property, however, relates to the fascinating optical properties of C-dots.^[4] Although its origin is still a question of debate,^[5] the strong and tunable fluorescence of C-dots is interesting with respect to their application in biomedicine, optoelectronics, catalysis, or sensing.^[6]

The synthesis of C-dots generally comprises three sequential steps starting with a temperature treatment of a carbon source, which is followed by a separation process, and a final surface functionalization.^[7] After their discovery, synthesis was most

often performed by physical methods and high-temperature treatment of coal, carbon black, graphite, carbon nanotubes, etc.^[8] Very quickly it has turned out that a thermal treatment of carbon-containing compounds is also suitable to obtain C-dots.^[9] This includes the thermal decomposition, for instance, of carbohydrates or amino acids.^[10] More curiously, but also suitable is the thermal treatment of, for instance, eggs, oranges, or leaves.^[11] Meanwhile, well-controlled access to C-dots is also possible via liquid-phase methods and most often involves the dehydration of carbohydrates by concentrated mineral acids (e.g. concentrated H_2SO_4),^[12] the thermal decomposition of multivalent alcohols (so-called polyols),^[13] or the thermal decomposition of carbohydrates in polyols.^[14] Moreover, surface functionalization of the as-prepared C-dots with polyols, and especially with polyethylene glycol (PEG) and its derivatives, is usually necessary to obtain sufficient fluorescence.^[4-6]

Despite various methods to obtain C-dots, a fully water-based synthesis of emissive C-dots is lacking so far. Such one-pot approach in water – including C-dot formation, colloidal stabilization, and surface functionalization – is realized in the following. Accordingly, $[\text{ZrO}]^{2+}$ $[\text{F6P}]^{2-}$ precursor nanoparticles (F6P: D-fructose-6-phosphate) are converted to blue-emitting C-dot@ $[\text{ZrO}]^{2+}$ $[\text{HPO}_4]^{2-}$ composite nanoparticles by boiling in water. This fully water-based synthesis can be also transferred to C-dot@ $[\text{Eu}(\text{OH})]^{2+}$ $[\text{HPO}_4]^{2-}$ composite nanoparticles that show intense Eu^{3+} -driven red emission in water. Our material composition compares to concepts with C-dots that were formed or embedded in porous materials such as zeolites or metalorganic frameworks.^[15] C-dot@ $[\text{ZrO}]^{2+}$ $[\text{HPO}_4]^{2-}$ and C-dot@ $[\text{Eu}(\text{OH})]^{2+}$ $[\text{HPO}_4]^{2-}$ composite nanoparticles, however, are obtained in a one-pot approach without the necessity of subsequent C-dot infiltration into a matrix, and they are non-porous with C-dots densely embedded in the phosphate matrix, which is advantageous in terms of a dispersion in water and a Eu^{3+} -based red emission in water.

[a] K. Sabljo, Prof. Dr. C. Feldmann
Institute for Inorganic Chemistry
Karlsruhe Institute of Technology (KIT)
Engesserstrasse 15, 76131 Karlsruhe (Germany)
Tel: (+)49-721-60842855
Fax: (+)49-721-60844892
E-mail: claus.feldmann@kit.edu

[b] Dr. R. Popescu, Prof. Dr. D. Gerthsen
Laboratory for Electron Microscopy
Karlsruhe Institute of Technology (KIT)
Engesserstrasse 7, 76131 Karlsruhe (Germany)

[c] Dr. N. C. Michenfelder, Prof. Dr. A.-N. Unterreiner
Institute of Physical Chemistry
Karlsruhe Institute of Technology (KIT)
Fritz-Haber-Weg 2, 76131 Karlsruhe (Germany)

Supporting information for this article is available on the WWW under <https://doi.org/10.1002/cnma.202100193>

© 2021 The Authors. ChemNanoMat published by Wiley-VCH GmbH. This is an open access article under the terms of the Creative Commons Attribution Non-Commercial NoDerivs License, which permits use and distribution in any medium, provided the original work is properly cited, the use is non-commercial and no modifications or adaptations are made.

2. Results and discussion

2.1. $[\text{ZrO}]^{2+}[\text{F6P}]^{2-}$ precursor nanoparticles

Aiming at nanomaterials for drug delivery and multimodal imaging, we have developed the concept of inorganic-organic hybrid nanoparticles (IOH-NPs).^[16] IOH-NPs have a general composition such as $[\text{ZrO}]^{2+}[\text{R}_{\text{Function}}\text{OPO}_3]^{2-}$, $[\text{LaO}]^{+}[\text{R}_{\text{Function}}\text{SO}_3]^{-}$, or $[\text{GdO}]^{+}[\text{R}_{\text{Function}}\text{COO}]^{-}$ ($\text{R}_{\text{Function}}$: drug and/or fluorescent dye) with an inorganic cation needed to make the IOH-NPs insoluble in water and a functional organic anion, which is a drug and/or a fluorescent dye. Specific examples include $[\text{ZrO}]^{2+}[\text{FdUMP}]^{2-}$ with the cytostatic agent 5'-fluoro-2'-deoxyuridine 5'-monophosphate (FdUMP),^[17] $[\text{ZrO}]^{2+}[\text{BMP}]^{2-}$ with the anti-inflammatory agent betamethasone phosphate (BMP),^[17,18] $[\text{ZrO}]^{2+}[\text{CLP}]^{2-}$ with the antibiotic agent clindamycin phosphate (CLP),^[19] or $[\text{GdO}]^{+}[\text{ICG}]^{-}$ with indocyanine green as infrared emitting dye (ICG).^[20] Aiming at the surface conditioning of such IOH-NPs, we also introduced phosphate-functionalized carbohydrate molecules such as D-fructose-6-phosphate ($[\text{F6P}]^{2-}$) as anions (Figure 1).

Initiated by this preliminary work, inorganic-organic hybrid nanoparticles with a composition $[\text{ZrO}]^{2+}[\text{F6P}]^{2-}$ could be realized by injection of an aqueous solution of $\text{ZrOCl}_2 \cdot 8\text{H}_2\text{O}$ into an aqueous solution of $\text{Na}_2[\text{F6P}]$ (Figure 1). Herein, $[\text{F6P}]^{2-}$ serves as the organic anion, which reacts to an insoluble compound in the presence of $[\text{ZrO}]^{2+}$ cations. In accordance with the La Mer-Dinegar model of particle nucleation and particle growth,^[21] a fast addition (injection) of $\text{ZrOCl}_2 \cdot 8\text{H}_2\text{O}$ under vigorous stirring and at slightly elevated temperature (40 °C) leads to a high supersaturation and results in the formation of small-sized particles. The formation of nanoparticles can be followed even with the naked eye and is indicated by the change of a transparent solution to a suspension showing light scattering (Figure 1). To remove all remaining salts and starting materials, the $[\text{ZrO}]^{2+}[\text{F6P}]^{2-}$ nanoparticles were twice centrifuged/redispersed in/from H_2O . Thereafter, they can be redispersed in water to obtain colloiddally stable aqueous suspensions, or they were dried at room temperature in air to obtain powder samples.

Particle size and particle size distribution of the $[\text{ZrO}]^{2+}[\text{F6P}]^{2-}$ precursor nanoparticles were examined via dynamic light scattering (DLS) (Figure 2a). The colloiddally stable aqueous

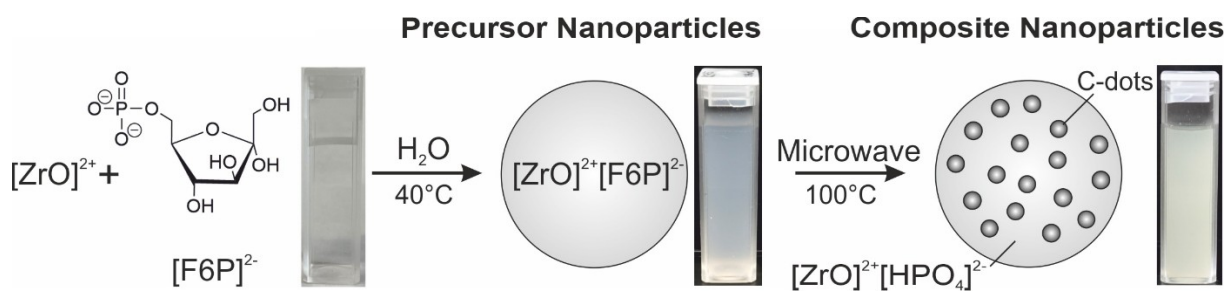


Figure 1. Illustration of the aqueous, one-pot synthesis of $[\text{ZrO}]^{2+}[\text{F6P}]^{2-}$ precursor nanoparticles and their conversion to phosphate-stabilized C-dot@ $[\text{ZrO}]^{2+}[\text{HPO}_4]^{2-}$ composite nanoparticles.

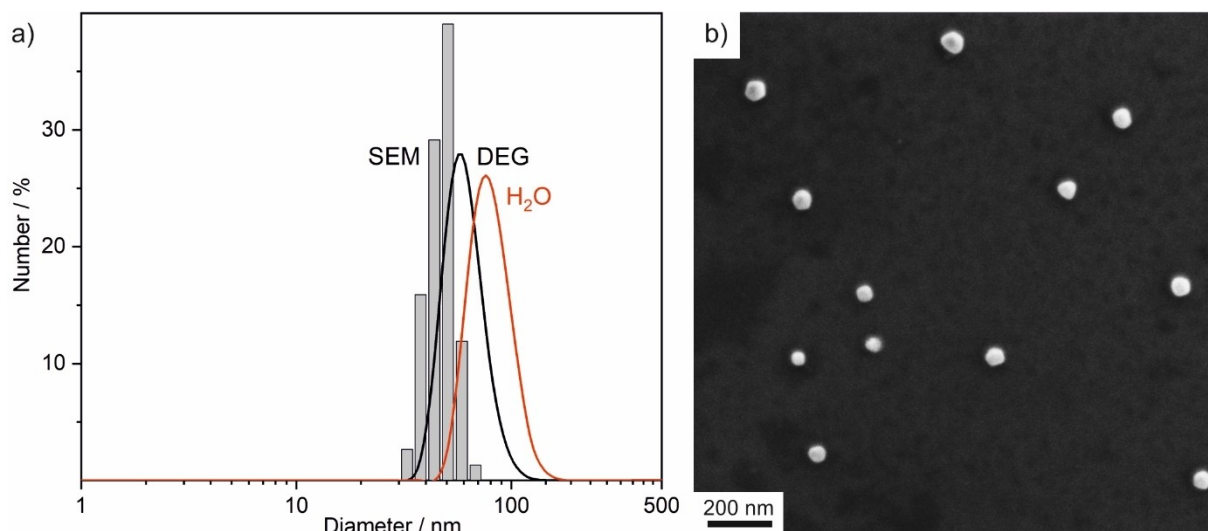
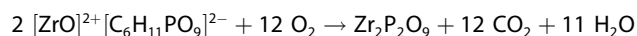


Figure 2. Particle size of $[\text{ZrO}]^{2+}[\text{F6P}]^{2-}$ precursor nanoparticles: a) Particle size distribution according to DLS analysis (in DEG and water) as well as according to statistical evaluation of 150 particles on SEM images; b) SEM image.

suspensions exhibit a mean hydrodynamic diameter of 80 ± 17 nm. In water, however, nanoparticles generally show larger hydrodynamic diameters due to the rigid layer of adsorbed solvent molecules.^[22] This view was confirmed after centrifugation and redispersion in diethylene glycol (DEG) as a less polar but more surface-active solvent. Herein, the mean diameter with 60 ± 12 nm is significantly smaller (Figure 2a). Scanning electron microscopy (SEM) shows the presence of spherical, non-agglomerated nanoparticles (Figure 2b). A statistical evaluation of 150 particles on SEM images results in a mean diameter of 48 ± 7 nm, which is well in agreement with the larger hydrodynamic diameters in DEG and H₂O obtained by DLS (Figure 2a).

According to X-ray powder diffraction (XRD), the $[\text{ZrO}]^{2+}[\text{F6P}]^{2-}$ precursor nanoparticles are non-crystalline and do not show any Bragg reflection (ESI: Figure S1). In fact, this is not a surprise and usually observed for water-based nucleation of inorganic-organic hybrid nanoparticles.^[17–21] To examine the chemical composition of the nanoparticles, different analytical techniques were used, including Fourier-transformed infrared spectroscopy (FT-IR), energy-dispersive X-ray spectroscopy (EDXS), thermogravimetry (TG), and elemental analysis (EA). FT-IR spectroscopy confirms the presence of $[\text{F6P}]^{2-}$ (Figure 3a). A comparison with the starting material Na₂[F6P] as a reference shows all characteristic vibrations of $[\text{F6P}]^{2-}$, including $\nu(\text{O-H})$: $3600\text{--}3000\text{ cm}^{-1}$, $\nu(\text{C-H})$: $3000\text{--}2800\text{ cm}^{-1}$, $\nu(\text{C=O})$: 1600 cm^{-1} , $\nu(\text{C-O})$: 1460 cm^{-1} , $\nu([\text{PO}_4]^{3-})$: $1100\text{--}900\text{ cm}^{-1}$. EDXS performed in a scanning electron microscope proves the presence of zirconium. A quantification of the EDXS data is not possible since the X-ray lines of zirconium and phosphorus overlap. The total organics content was obtained by TG (Figure 3b). Thus, dried $[\text{ZrO}]^{2+}[\text{F6P}]^{2-}$ nanoparticles show a weight loss of 43.8% up to a temperature of 1200 °C, which is in good agreement with the calculated weight loss of 43.9% for the total organics combustion of the assumed composition $[\text{ZrO}]^{2+}[\text{F6P}]^{2-}$. The thermal residue was identified via XRD to be Zr₂P₂O₉ with traces of ZrO₂ (ESI: Figure S2). Accordingly, the thermal combustion reaction can be rationalized as follows:



Finally, the composition was verified by EA, resulting in C/H contents of 18.1 wt-% C and 2.6 wt-% H (calculated: 19.7 wt-% C, 3.0 wt-% H). Since the organics content is encapsulated by the phosphate during combustion similar to the effect of phosphate-based flame retardants, the observed C/H contents are slightly lower as the calculated values. All-in-all, these results confirm a 1:1 ratio of zirconyl cation and carbohydrate-type anion, and thus, a composition $[\text{ZrO}]^{2+}[\text{F6P}]^{2-}$ of the as-prepared precursor nanoparticles.

2.2. Conversion to C-dot@[ZrO]²⁺[HPO₄]²⁻ composite nanoparticles

In principle, the caramelization of carbohydrates is well-known, but either requires a separation of C-dots from other carbon remains and/or highly viscous solvents (e.g. polyols) as well as a distinct surface functionalization.^[10,12,14] These procedures are so far essential pre-requisites to obtain dispersible C-dots that show considerable fluorescence in water. The concept of carbohydrate-containing precursor nanoparticles such as $[\text{ZrO}]^{2+}[\text{F6P}]^{2-}$ and their instantaneous conversion to C-dots in a stabilizing matrix – to the best of our knowledge – has not been suggested till now. Although this synthesis strategy can be also performed with other carbohydrate-containing IOH-NPs, D-fructose-6-phosphate seemed most promising since fructose is known for its easy dehydration at low temperature.^[23] Already during the synthesis of $[\text{ZrO}]^{2+}[\text{F6P}]^{2-}$ at 40 °C, a light yellow color indicates the beginning decomposition, which is already accompanied by weak bluish fluorescence (ESI: Figure S3). Since neither zirconyl cations nor D-fructose-6-phosphate anions show any fluorescence, the occurring weak emission must be attributed to a beginning decomposition of $[\text{F6P}]^{2-}$ with formation of C-dots. The formation of C-dots by thermal decomposition of fructose was promoted by microwave heating

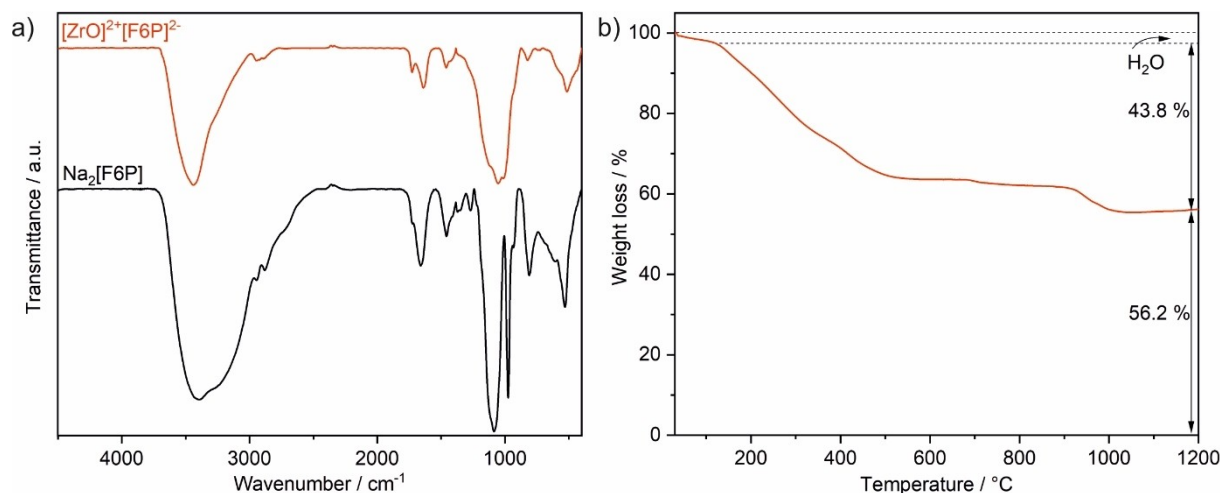


Figure 3. Chemical composition of $[\text{ZrO}]^{2+}[\text{F6P}]^{2-}$ precursor nanoparticles: a) FT-IR spectra (Na₂[F6P] as a reference); b) TG analysis.

of the aqueous suspension (25 min, 100 °C, Figure 1). In this regard, microwave heating allows a very fast heating and, thereby, a rapid dehydration and carbonization. The advantage of $[\text{ZrO}]^{2+}[\text{F6P}]^{2-}$ in comparison to pure fructose relates to the facts that the nanoregime is already established with the precursor nanoparticles and that the carbon source and stabilizing phosphate-matrix are already available in the precursor nanoparticles. Moreover, it needs to be noticed that a direct decomposition of fructose phosphate results in significantly larger C-dots (> 10 nm) that only show weak emission in water (ESI: Figures S4–S7).

Subsequent to microwave heating, the resulting aqueous C-dot@ $[\text{ZrO}]^{2+}[\text{HPO}_4]^{2-}$ suspensions exhibit mean hydrodynamic diameters of 83 ± 17 nm in H_2O and 65 ± 11 nm in DEG as well as a mean diameter of 43 ± 10 nm according to a statistical evaluation of 100 particles on SEM images (Figure 4a,b). These data are in agreement with the $[\text{ZrO}]^{2+}[\text{F6P}]^{2-}$ precursor nanoparticles (Figure 2a,b). In difference to the weak yellow color of

$[\text{ZrO}]^{2+}[\text{F6P}]^{2-}$, aqueous suspensions as well as powder samples of the C-dot@ $[\text{ZrO}]^{2+}[\text{HPO}_4]^{2-}$ nanoparticles exhibit a bright yellow color (Figure 4c). Even more interesting, both aqueous suspensions and powder samples show intense emission of blue light (Figure 4c,d). The emission can be quantified based on fluorescence spectra. Thus, aqueous suspensions of C-dot@ $[\text{ZrO}]^{2+}[\text{HPO}_4]^{2-}$ show broad absorption at 300–400 nm with its maximum at 350 nm (Figure 4e; SI: Figure S8). Emission occurs at 400–650 nm. The observed luminescence features already indicate the presence of C-dots. Particularly characteristic is the dependence of the emission on the wavelength of the excitation and the resulting red-shift with decreasing emission intensity at increasing wavelength of excitation (Figure 4e).^[4] Here, it must be noticed the amorphous $[\text{ZrO}]^{2+}[\text{HPO}_4]^{2-}$ matrix material (without C-dots) does not show any specific fluorescence (ESI: Figures S9, S10).

To prove the formation of C-dots and to examine the structure of the composite nanoparticles formed by thermal

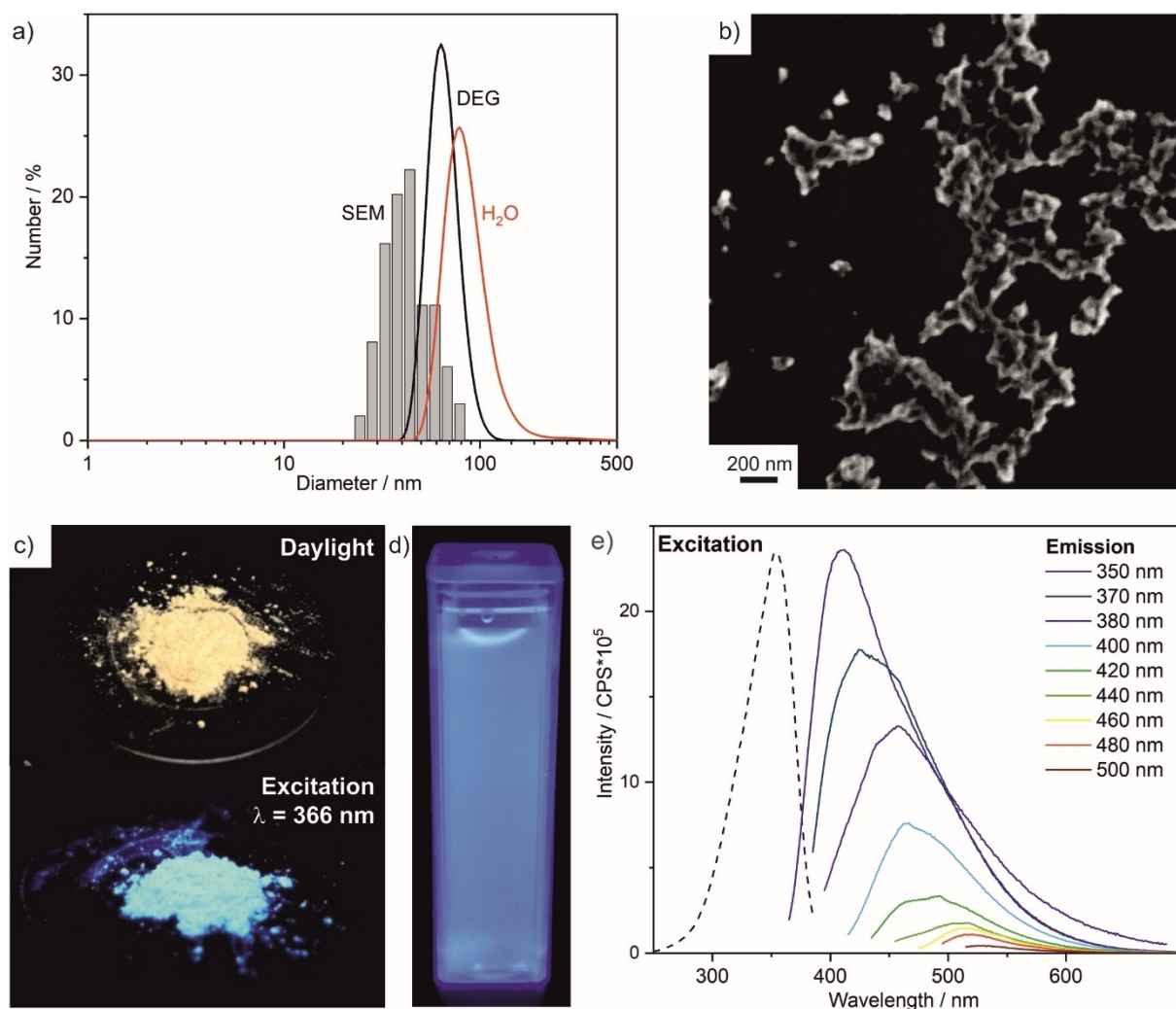


Figure 4. Size and luminescence of C-dot@ $[\text{ZrO}]^{2+}[\text{HPO}_4]^{2-}$ composite nanoparticles: a) Particle size distribution according to DLS analysis (in DEG and water) as well as according to statistical evaluation of 100 particles on SEM images; b) SEM image; c) Powder samples under daylight and with excitation (366 nm); d) Aqueous suspension with 366 nm excitation; e) Fluorescence spectra of aqueous suspensions with excitation ($\lambda_{em} = 400$ nm) and emission at different excitation wavelengths.

decomposition of the $[\text{ZrO}]^{2+}[\text{F6P}]^{2-}$ precursor nanoparticles, the yellow C-dot@ $[\text{ZrO}]^{2+}[\text{HPO}_4]^{2-}$ composite nanoparticles were separated via centrifugation. Thereafter, different analytical methods were consulted, including transmission electron microscopy (TEM), energy-dispersive X-ray spectroscopy (EDXS), fluorescence spectroscopy, infrared spectroscopy (FT-IR, SI: Figure S4), nuclear magnetic resonance spectroscopy (NMR, SI: Figure S5) and ultraviolet-visible spectroscopy (UV-Vis, SI: Figure S6). FT-IR, NMR, and UV-Vis spectroscopy already point to the formation of C-dots through thermal decomposition of $\text{Na}_2[\text{F6P}]$. These C-dots, however, are significantly larger (15–20 nm), and they show only very weak emission in water (ESI: Figure S7). High-angle annular dark-field (HAADF) STEM overview images of C-dot@ $[\text{ZrO}]^{2+}[\text{HPO}_4]^{2-}$ composite nanoparticles indeed show a complex heterogeneous structure (Figure 5a). Herein, the light areas indicate the presence of strongly scattering material containing high-weight atoms, whereas the darker regions indicate a material with lower-weight atoms. These dark regions have diameters of 2–3 nm, which is a typical size of C-dots. EDXS linescans along the red line in Figure 5a show strongly fluctuating element concentrations of Zr, P, O, and C (Figure 5d) and confirm the presence of strongly and

weakly scattering material. As-expected, the dark regions show carbon as dominating element (Figure 5d: black line), whereas the matrix in between exhibits high concentrations of Zr, P and O. EDXS also indicates a 1:1 ratio of Zr and P, which again confirms the composition of the composite nanoparticles. Based on the electron microscopic data, moreover, the C-dot: $[\text{ZrO}]^{2+}[\text{HPO}_4]^{2-}$ volume ratio can be estimated to 20:80. Finally, high-resolution (HR)-TEM images of C-dots near the surface show distinct lattices fringes (Figure 5b). The Fourier-transformed HRTEM image of the C-dots (Figure 5c) is compatible with the bulk graphite structure (space group: $P6_3/mmc$, lattice parameters: $a=2.460 \text{ \AA}$, $c=6.704 \text{ \AA}$) in $[211]$ zone-axis orientation.^[24] All-in-all, this proves the presence of highly crystalline C-dots encapsulated in a $[\text{ZrO}]^{2+}[\text{HPO}_4]^{2-}$ matrix.

2.3. Red-emitting C-dot@ $[\text{Eu}(\text{OH})]^{2+}[\text{HPO}_4]^{2-}$ composite nanoparticles

Based on the results of the $[\text{ZrO}]^{2+}[\text{F6P}]^{2-}$ and C-dot@ $[\text{ZrO}][\text{HPO}_4]$ nanoparticles, we have considered to obtain red-emitting C-dot nanoparticles via a similar approach (Figure 1).

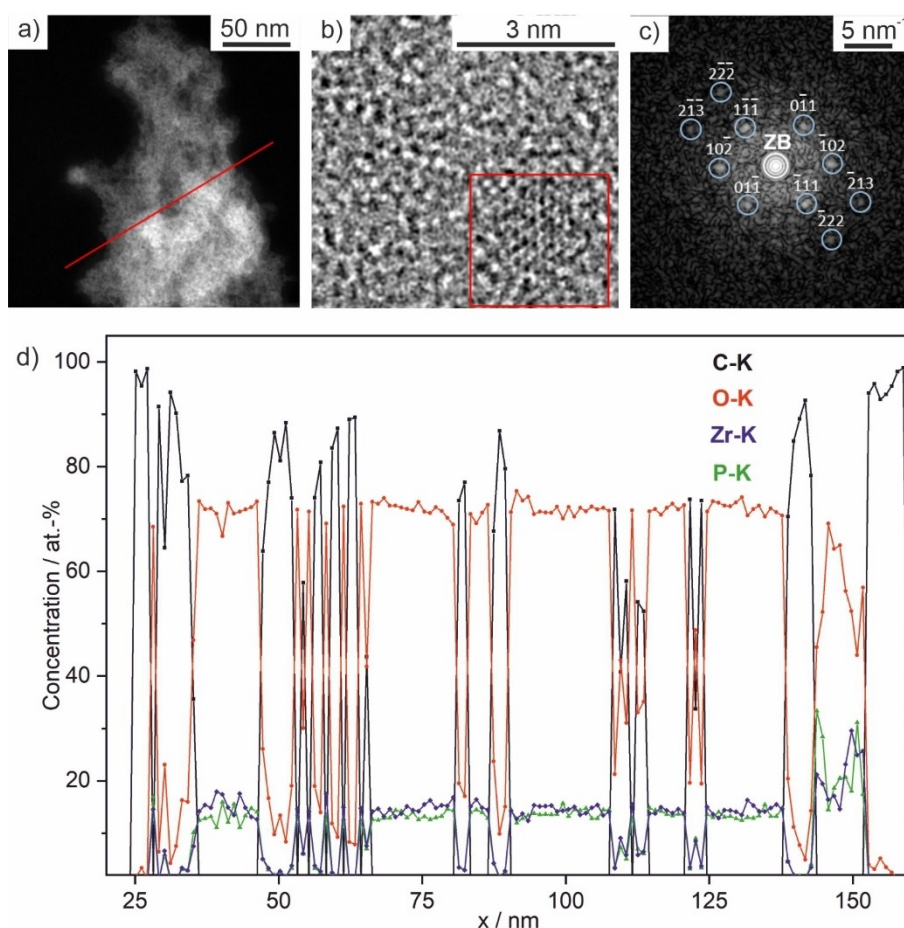


Figure 5. Structure and composition of C-dot@ $[\text{ZrO}]^{2+}[\text{HPO}_4]^{2-}$ composite nanoparticles: a) HAADF-STEM image; b) HRTEM image of encapsulated C-dot with lattice fringes; c) Fourier-transformed HRTEM image of C-dot in $[211]$ zone-axis orientation with indexed Bragg reflections (ZB marks the zero-order beam); d) EDXS line scan (black: C ($\text{O}-K_{\alpha}$), red: O ($\text{O}-K_{\alpha}$), blue: Zr ($\text{Zr}-L_{\alpha}$), green: P ($\text{P}-K_{\alpha}$)).

Red emission is of particular relevance for biomedical applications due to the significantly higher tissue penetration of red light in comparison to light of shorter wavelength.^[25] Aiming at red light, the characteristic line-type emission of Eu^{3+} , predominantly at 614 and 695 nm, is well known.^[26] However, the parity-forbidden $f-f$ -transitions on Eu^{3+} are typically quenched under aqueous conditions due to competitive relaxation via O–H vibrations.^[27] With this background, we have intended to realize precursor nanoparticles by combining $[\text{Eu}(\text{OH})]^{2+}$ (instead of $[\text{ZrO}]^{2+}$) as inorganic cation with fructose phosphate ($[\text{F6P}]^{2-}$) as carbohydrate-type anion. Similar to $[\text{ZrO}]^{2+}[\text{F6P}]^{2-}$, the injection of an aqueous solution of $\text{EuCl}_3 \cdot 6\text{H}_2\text{O}$ into a solution of $\text{Na}_2[\text{F6P}]$ resulted in the formation of precursor nanoparticles with a composition $[\text{Eu}(\text{OH})]^{2+}[\text{F6P}]^{2-}$ (Figure 6a). According to DLS, they exhibit mean hydrodynamic diameters of 84 ± 19 nm in H_2O and 55 ± 11 nm in DEG (Figure 6a). SEM confirms the presence of spherical nanoparticles with a mean diameter 50 ± 13 nm (based on a statistical evaluation of 100 particles, Figure 6b).

The chemical composition of the $[\text{Eu}(\text{OH})]^{2+}[\text{F6P}]^{2-}$ precursor nanoparticles was again validated by EDXS and FT-IR spectroscopy, which confirm the presence of europium and F6P (ESI: Figure S11a). For quantification, TG and EA were employed and showed a weight loss of 41.8% due to total organics combustion as well as C/H contents of 16.3 wt-% C and 1.6 wt-% H, which are again slightly lower than the expected values due to the encapsulation of the organics content in the phosphate matrix (calculated total organics combustion: 42.2%, SI: Figure S11b; calculated C/H content: 16.8 wt-% C, 2.8 wt-% H). According to XRD, EuPO_4 was obtained as thermal remnant of the TG analysis (ESI: Figure S12). Similar to $[\text{ZrO}]^{2+}[\text{F6P}]^{2-}$, precursor nanoparticles with 1:1 ratio of europium cation and carbohydrate-type anion were obtained as expressed by the formula $[\text{Eu}(\text{OH})]^{2+}[\text{F6P}]^{2-}$.

In the case of $[\text{Eu}(\text{OH})]^{2+}[\text{F6P}]^{2-}$, the conversion to C-dot@ $[\text{Eu}(\text{OH})]^{2+}[\text{HPO}_4]^{2-}$ nanoparticles can be also initiated and

followed by fs-transient absorption spectroscopy (Figure 7a). Thus, laser-driven excitation at 267 and 400 nm resulted in comparable transient spectra for single transient excerpts at probe wavelengths of 350 (i.e. emission of C-dot) and 460 nm (i.e. emission of Eu^{3+}) and a slow rise within 2 ps (Figure 7b). In contrast, solutions of $\text{Na}_2[\text{F6P}]$ as a reference show quasi-instantaneous population with a long lifetime up to the ns regime after 267 nm excitation (ESI: Figures S13, S14). The transient response does not recover within the experimental time window of 1 ns. The slower rise of the $[\text{Eu}(\text{OH})]^{2+}[\text{F6P}]^{2-}$ suspension compared to the $\text{Na}_2[\text{F6P}]$ reference solution may indicate a more complex energy distribution within the nanoparticle before reaching the luminescent state. Interestingly, transient spectra after 267 nm excitation show a shorter lifetime of few hundred ps (ESI: Figures S13, S14), which supports this assignment as well as a negligible intensity of luminescence in the UV range. Please note that the narrow Eu^{3+} emission lines cannot be observed under these conditions. Moreover, it needs to be noticed that transient absorption spectroscopy of C-dot@ $[\text{Eu}(\text{OH})]^{2+}[\text{HPO}_4]^{2-}$ composite nanoparticles failed due to dominant light scattering. In sum, transient absorption spectroscopy as well as UV-Vis spectra indicate the successful incorporation of Eu^{3+} into the nanoparticles.

As next step, the $[\text{Eu}(\text{OH})]^{2+}[\text{F6P}]^{2-}$ precursor nanoparticles were as well thermally decomposed by microwave heating of aqueous suspensions at 100 °C. Subsequent to the decomposition, TEM was used to evidence the structure of the resulting composite nanoparticles and to prove the presence of C-dots (Figure 8). Similar to C-dot@ $[\text{ZrO}]^{2+}[\text{HPO}_4]^{2-}$, HAADF-TEM images of the here obtained composite C-dot@ $[\text{Eu}(\text{OH})]^{2+}[\text{HPO}_4]^{2-}$ nanoparticles show a structure with light areas indicating high-weight atoms and darker regions indicating low-weight atoms (Figure 8a). The dark regions with sizes of 2–3 nm are again typical for C-dots. EDXS linescans along the red line in Figure 8a show the expected strongly fluctuating element concentration and evidence the matrix to predominately contain Eu, P, O,

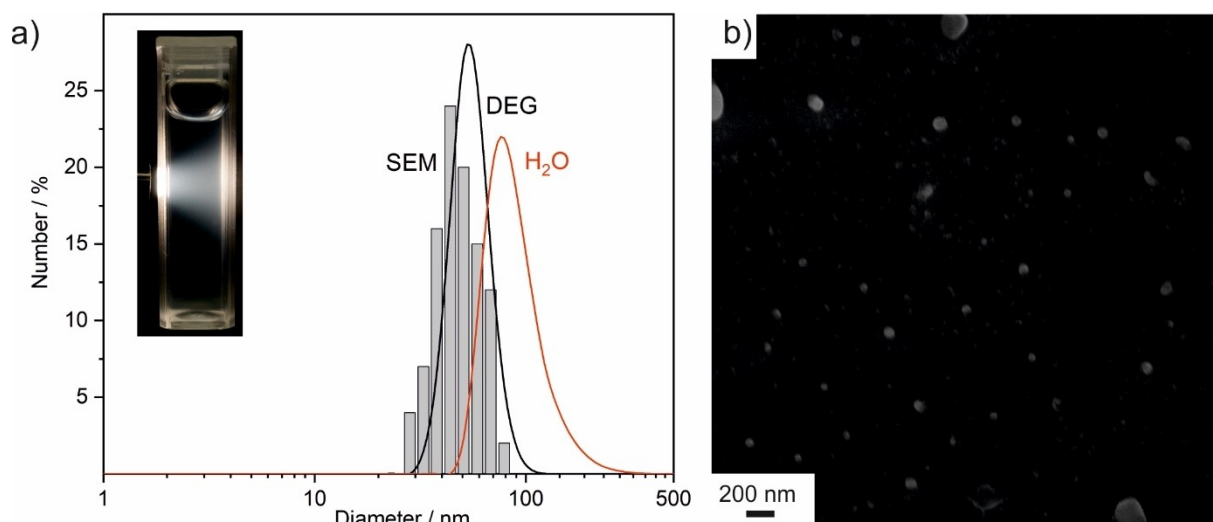


Figure 6. Particle size of $[\text{Eu}(\text{OH})]^{2+}[\text{F6P}]^{2-}$ precursor nanoparticles: a) Particle size distribution according to DLS analysis (in DEG and water) as well as according to statistical evaluation of 100 particles on SEM images with inset of a photo of an aqueous suspension; b) SEM image.

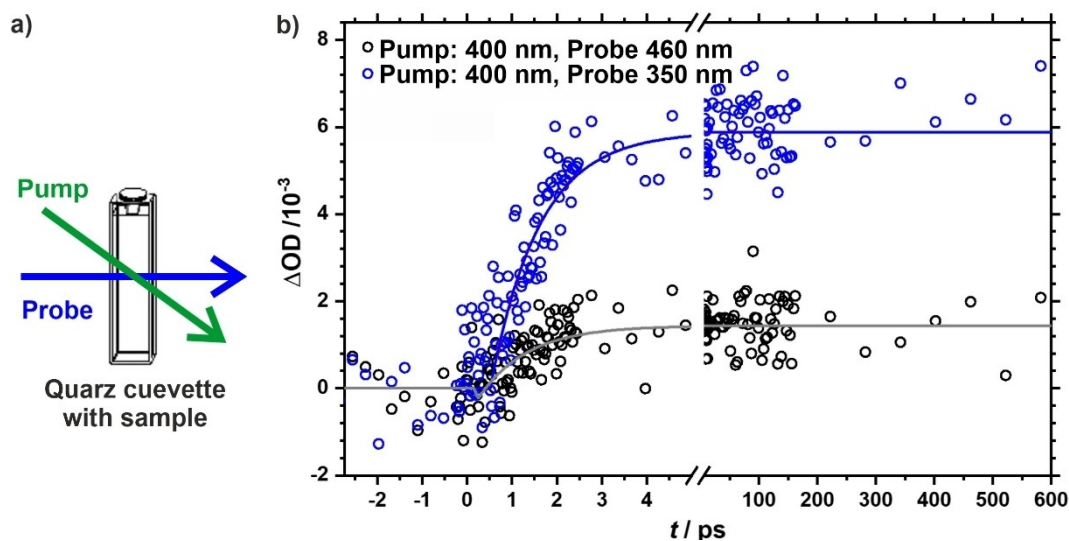


Figure 7. Transient absorption traces for $[\text{Eu}(\text{OH})]^{2+}[\text{F6P}]^{2-}$ precursor nanoparticles in aqueous suspension at 350 and 460 nm probe wavelengths after excitation at 400 nm (symbols) and fit curves (lines) from global analysis (OD: optical density) (see ESI).

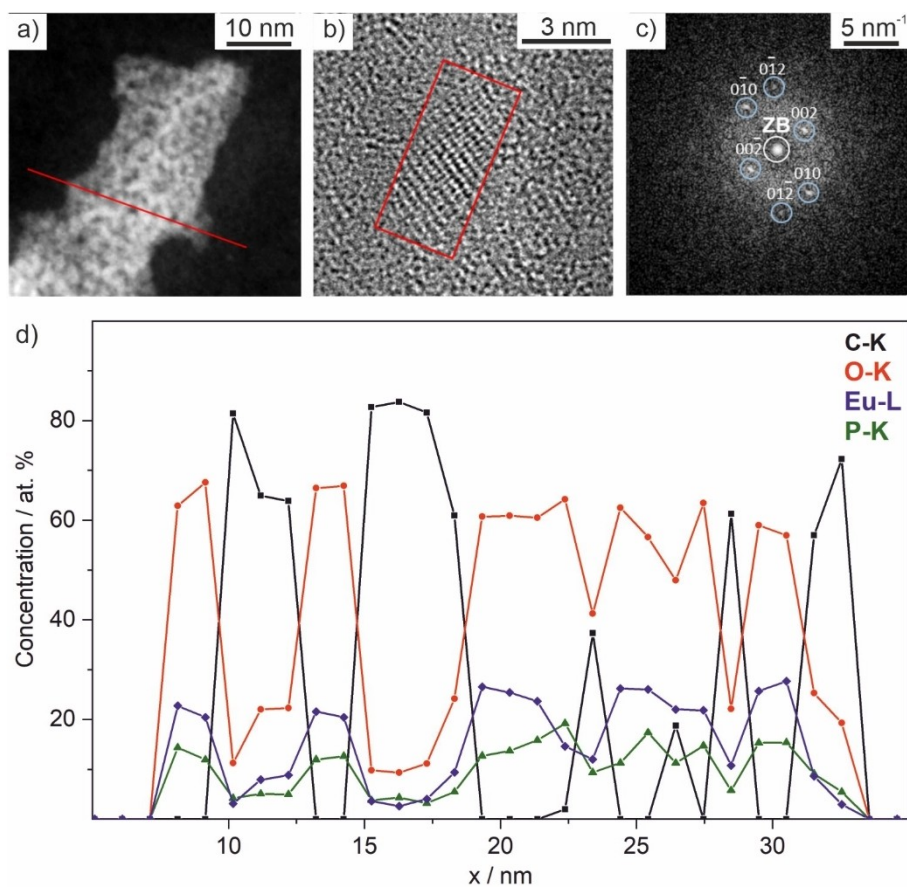


Figure 8. Structure and composition of C-dot@[$\text{Eu}(\text{OH})]^{2+}[\text{HPO}_4]^{2-}$ composite nanoparticles: a) HAADF-STEM image; b) HRTEM image of encapsulated C-dot with lattice fringes; c) FT-HRTEM image of C-dot in [100] zone-axis orientation with indexed Bragg reflections (ZB marks the zero-order beam); d) EDXS line (black: C (O- K_{α}), red: O (O- K_{α}), blue: Eu (Eu- $L_{\alpha 1}$) line, green: P (P- K_{α})).

whereas the dark regions contain C as dominating element (Figure 8d). EDXS also indicates a 1:1 ratio of Eu and P, which

confirms the composition of the composite nanoparticles. The C-dot: $[\text{Eu}(\text{OH})]^{2+}[\text{HPO}_4]^{2-}$ volume ratio can be again estimated

to about 20:80. The presence of C-dots was further validated by HRTEM images, which show distinct lattices fringes (Figure 8b).^[24] The Fourier-transformed HRTEM image of the particle is compatible with bulk graphite in [100] zone-axis orientation (Figure 8c). In sum, the nanoparticles can be concluded to contain highly crystalline C-dots encapsulated in a $[\text{Eu}(\text{OH})]^{2+}[\text{HPO}_4]^{2-}$ matrix as expressed by the description C-dot@[$\text{Eu}(\text{OH})]^{2+}[\text{HPO}_4]^{2-}$. In difference to totally amorphous C-dot@[$\text{ZrO}^{2+}[\text{HPO}_4]^{2-}$, XRD analysis of the C-dot@[$\text{Eu}(\text{OH})]^{2+}[\text{HPO}_4]^{2-}$ composite nanoparticles shows few Bragg reflections that indicate certain crystallinity (ESI: Figure S15). These Bragg reflections are of course broad and low in intensity, which is not a surprise when considering the low synthesis temperature (100 °C). A comparison with the most intense Bragg reflections of bulk- EuPO_4 as a reference suggests certain similarity, which is further confirmed after heating (ESI: Figure S15).

Finally, the optical properties of the C-dot@[$\text{Eu}(\text{OH})]^{2+}[\text{HPO}_4]^{2-}$ nanoparticles were examined by UV-Vis and fluorescence spectroscopy. The most important result is already visible with the naked eye. Thus, powder samples as well as aqueous suspensions clearly show red emission (Figure 9a,c). Excitation spectra recorded at maximum emission of the C-dots ($\lambda_{em}=365$ nm) show broad C-dot-related absorption (250–

350 nm). Excitation spectra recorded at maximum emission of Eu^{3+} ($\lambda_{em}=615$ nm) show the characteristic $f \rightarrow f$ transitions and prove the presence of Eu^{3+} (Figure 9b). Emission spectra were recorded at different excitation wavelengths and show broad C-dot-related emission at 350–450 nm (Figure 9d). Most interesting, the characteristic Eu^{3+} emission lines are visible for all types of excitation, and naturally most intense if the excitation was performed on Eu^{3+} itself (e.g. at 394 nm). The most intense emission lines of Eu^{3+} at 615 and 695 nm, however, are visible for all types of excitation. This finding is most relevant since these parity-forbidden $f \rightarrow f$ transitions are typically quenched in the presence of water.^[26,27] In this respect, the observation of Eu^{3+} -related red emission also points to certain crystallinity of the $[\text{Eu}(\text{OH})]^{2+}[\text{HPO}_4]^{2-}$ matrix, which was already suggested by XRD. The observation of Eu^{3+} -based red emission in aqueous suspension, on the one hand, proves the successful energy transfer from C-dots to Eu^{3+} in the $[\text{Eu}(\text{OH})]^{2+}[\text{HPO}_4]^{2-}$ matrix, and on the other hand, the efficient shielding of Eu^{3+} in the matrix from vibrational quenching processes. Finally, it needs to be noticed that the $[\text{Eu}(\text{OH})]^{2+}[\text{HPO}_4]^{2-}$ matrix material (without any C-dots) also shows Eu^{3+} -related luminescence, naturally without any contribution from C-dots (ESI: Figures S16, S17).

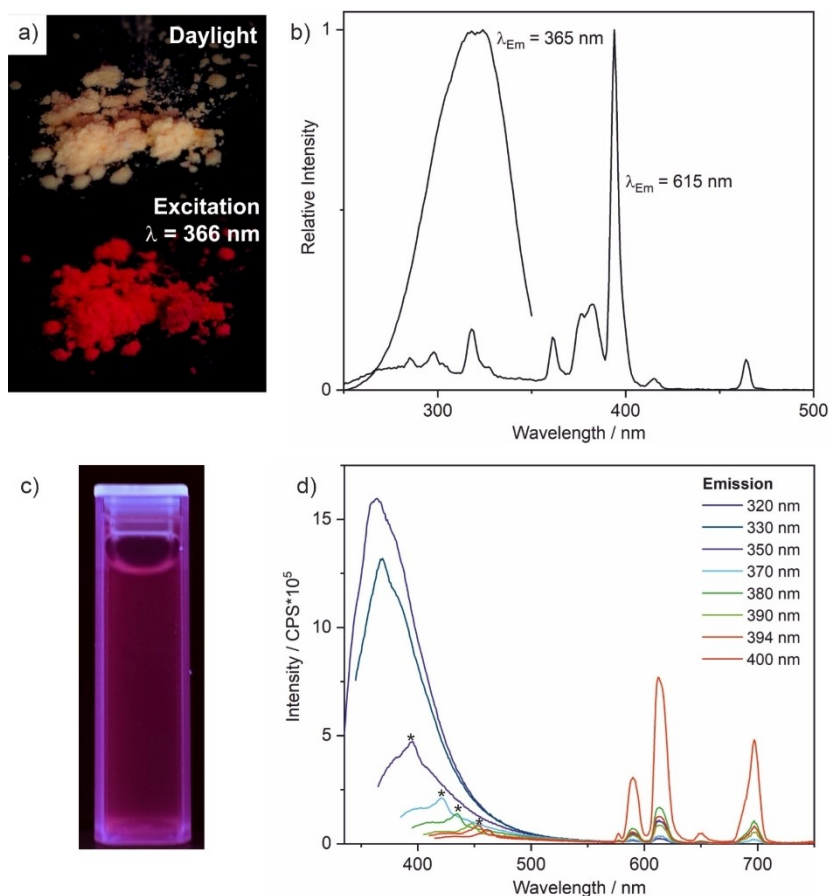


Figure 9. Luminescence of C-dot@[$\text{Eu}(\text{OH})]^{2+}[\text{HPO}_4]^{2-}$ composite nanoparticles: a) Powder samples under daylight and with excitation (366 nm); b) Excitation spectra of aqueous suspensions, c) Photo of aqueous suspension with 366 nm-excitation; d) Emission spectra of aqueous suspensions with excitation at different wavelengths (*Raman scattering of water visible as low intensity emission).

3. Conclusion

Aiming at a fully water-based one-pot synthesis of emissive C-dots, C-dot@[ZrO]₂²⁺[HPO₄]₄²⁻ and C-dot@[Eu(OH)]₃²⁺[HPO₄]₄²⁻ composite nanoparticles were realized via [ZrO]₂²⁺[F6P]²⁻ or [Eu(OH)]₃²⁺[F6P]²⁻ precursor nanoparticles. The synthesis concept starts with the formation of insoluble [ZrO]₂²⁺[F6P]²⁻ or [Eu(OH)]₃²⁺[F6P]²⁻ precursor nanoparticles after injecting a solution of ZrOCl₂·8H₂O or EuCl₃·6H₂O into a solution of Na₂[F6P] (F6P: D-fructose-6-phosphate). The resulting [ZrO]₂²⁺[F6P]²⁻ and [Eu(OH)]₃²⁺[F6P]²⁻ precursor nanoparticles exhibit mean particle diameters of 43 ± 10 and 50 ± 13 nm, respectively.

The aqueous suspension of the precursor nanoparticles was instantaneously converted to C-dot@[ZrO]₂²⁺[HPO₄]₄²⁻ and C-dot@[Eu(OH)]₃²⁺[HPO₄]₄²⁻ composite nanoparticles in boiling water via microwave heating. The mean particle diameter (43 ± 10 nm) of the composite nanoparticles is very comparable to the precursor nanoparticle and points the instantaneous conversion. Electron microscopy and electron spectroscopy elucidate the structure of the C-dot@[ZrO]₂²⁺[HPO₄]₄²⁻ and C-dot@[Eu(OH)]₃²⁺[HPO₄]₄²⁻ composite nanoparticles with highly crystalline C-dots (2–3 nm in size) encapsulated in a [ZrO]₂²⁺[HPO₄]₄²⁻ or [Eu(OH)]₃²⁺[HPO₄]₄²⁻ matrix. These C-dot@[ZrO]₂²⁺[HPO₄]₄²⁻ and C-dot@[Eu(OH)]₃²⁺[HPO₄]₄²⁻ composite nanoparticles show intense blue and red emission in water. The novel water-based synthesis strategy and the resulting composite structure now can be a subject for further variation and might specifically become interesting for biomedical applications.

Experimental Section

Synthesis details

[ZrO]₂²⁺[F6P]²⁻ precursor nanoparticles. In a first step, 50 mg of D-fructose-6-phosphate disodium salt (Na₂[F6P], Biomol, 98%) were dissolved in 50 mL of demineralized water. This solution was heated to 40 °C and stirred vigorously. Thereafter, 0.5 mL of an aqueous solution containing 50.4 mg of ZrOCl₂·8H₂O (Sigma Aldrich, 99%) was injected. The instantaneous formation of [ZrO]₂²⁺[F6P]²⁻ nanoparticles is indicated by the change of a transparent solution to a colorless suspension, showing the expected light scattering of nanoparticles. After 2 min of intense stirring, the nanoparticles were separated via centrifugation (25000 rpm, 15 min). To remove all remaining salts, the [ZrO]₂²⁺[F6P]²⁻ nanoparticles were centrifuged/redispersed two times in/from H₂O. Finally, the [ZrO]₂²⁺[F6P]²⁻ precursor nanoparticles were redispersed in 20 mL of demineralized water.

C-dot@[ZrO]₂²⁺[HPO₄]₄²⁻ composite nanoparticles. An aqueous suspension of redispersed [ZrO]₂²⁺[F6P]²⁻ nanoparticles was heated to 100 °C by microwave treatment (25 min, 800 W). During heating, the color of the suspension turned from colorless to yellow, which indicates the proceeding decomposition of [F6P]²⁻ and the formation of C-dots. The resulting C-dot@[ZrO]₂²⁺[HPO₄]₄²⁻ nanoparticles were separated via centrifugation (25000 rpm, 15 min). For purification, the nanoparticles were resuspended/centrifuged in/from H₂O. For analytical characterization, the C-dot@[ZrO]₂²⁺[HPO₄]₄²⁻ nanoparticles were dried to a powder samples or redispersed in water.

C-dot@[Eu(OH)]₃²⁺[HPO₄]₄²⁻ composite nanoparticles. The synthesis was performed similarly to the aforementioned C-dot@[ZrO]₂²⁺[HPO₄]₄²⁻ nanoparticles. Thus, 50 mg of D-fructose-6-phosphate disodium salt (Na₂[F6P], Biomol, 98%) were dissolved in 50 mL of demineralized water. This solution was heated to 40 °C and stirred vigorously. Thereafter, 0.5 mL of an aqueous solution containing 57.4 mg of EuCl₃·6H₂O (Sigma Aldrich, 99%) were injected, followed by an addition of 2.5 mL of 0.1 M NaOH to increase the pH to a value of 7. After 2 min of intense stirring, the resulting nanoparticles were separated via centrifugation (25000 rpm, 15 min) and washed twice by redispersion/centrifugation in/from H₂O. After redispersion in water, the nanoparticles were heated to 100 °C by microwave treatment (25 min, 800 W) and converted to C-dot@[Eu(OH)]₃²⁺[HPO₄]₄²⁻ nanoparticles. Separation and purification were then performed as described before.

Na₂[F6P] reference sample. 25 mg of D-fructose-6-phosphate disodium salt (Na₂[F6P], Biomol, 98%) were dissolved in 25 mL of demineralized water and heated to 100 °C by microwave treatment (25 min, 800 W). The yellow color of the suspension indicated the proceeding decomposition of Na₂[F6P] and the formation of the C-dots. The as-prepared highly stable C-dot suspension can be destabilized by addition of an excess of acetone with a ratio of 5:1. After sedimentation, the as-prepared C-dots also can be easily separated from non-decomposed Na₂[F6P], which remained in solution. After decantation and evaporation of the solvent, a yellow powder was obtained. It needs to be noticed that C-dots obtained by direct decomposition of Na₂[F6P] are significantly larger in diameter (> 10 nm) and show only weak emission in water (ESI).

Analytical methods

Dynamic light scattering (DLS) was used to determine the hydrodynamic diameter of the nanoparticles and their size distribution in suspension. Measurements were performed in polystyrene cuvettes applying a Nanosizer ZS (Malvern Instruments, United Kingdom).

Scanning electron microscopy (SEM) was carried out with a Zeiss Supra 40 VP (Zeiss, Germany) with a field emission gun (acceleration voltage 5 kV, working distance 3 mm). Samples were prepared by placing a droplet of diluted aqueous suspension on a silica wafer.

Energy-dispersive X-ray spectroscopy (EDXS) was performed with an Ametek EDAX system (Ametec, USA) mounted on a Zeiss SEM Supra 35 VP scanning electron microscope. For EDXS analysis, the nanoparticles were pressed to dense pellets and fixed with conductive carbon pads on aluminum sample holders. EDXS was only used to validate the presence of zirconium and phosphorus since light elements (H, C, N, O) cannot be reliably quantified.

Transmission electron microscopy (TEM), high-angle annular dark-field scanning transmission electron microscopy (HAADF-STEM), and energy dispersive X-ray spectroscopy (EDXS) were conducted with a FEI Tecnai Osiris microscope (FEI, USA) at 200 keV electron energy, equipped with a Super-X EDXS system comprising four silicon drift detectors. High-resolution transmission electron microscopy (HRTEM) was performed with an aberration-corrected FEI Titan³ 80–300 microscope operated at 300 keV electron energy. TEM samples of the as-prepared C-dots were prepared by vacuum evaporation of aqueous suspensions at 50 °C on ultrathin amorphous carbon films (3 nm) mounted on amorphous carbon (lacey-) film-coated copper grids.

Fourier-transformed infrared spectra (FT-IR) were recorded with a Bruker Vertex 70 FT-IR spectrometer (Bruker, Germany) in the range 4000–400 cm⁻¹ with a resolution of 4 cm⁻¹. 1–1.5 mg of the dried sample were pestled with 300 mg of KBr and pressed to a pellet.

X-ray powder diffraction (XRD) measurements were conducted with a STADI-P diffractometer (Stoe, Germany) with Ge-monochromatized Cu-K α -radiation ($\lambda = 1.54278 \text{ \AA}$) and Debye-Scherrer geometry. The transmission samples were placed on sodium acetate foils and fixed with an amorphous adhesive film.

Thermogravimetry (TG) was performed with a STA409 C device (Netzsch, Germany). The vacuum-dried nanoparticles (20–30 mg) were heated to 1200 °C with a rate of 1 K/min in air.

Elemental analysis (EA, C/H/N/S analysis) was performed via thermal combustion with an Elementar Vario Micro Cube (Elementar, Germany) at a temperature of 1100 °C.

Fluorescence spectroscopy (FL). Excitation and emission spectra were recorded with a resolution of $\pm 1 \text{ nm}$ using a photoluminescence spectrometer Spex Fluorolog 3 (Horiba Jobin Yvon, France), equipped with a 450 W Xe-lamp and double monochromators.

Stationary absorption spectra. Absorption spectra were obtained with an UV/Vis/NIR spectrometer Cary 500 (Varian) in aqueous suspension in a wavelength range between 200 and 2000 nm. Spectra were measured at room temperature in cuvettes made of fused silica (Hellma) with 1 mm optical path length.

Transient absorption spectra. An experimental setup of the apparatus for obtaining transient spectra in the UV-Vis spectral regime is described elsewhere.^[28] Briefly, one small part of the 800 nm (Astrella (Coherent), 7 mJ, 35 fs, repetition rate 1 kHz) laser output was focused into a movable 2 mm CaF₂ crystal (Nortus Optronic GmbH) to generate a white-light continuum between 350 and 720 nm. After passing the sample, the white-light is refracted by a fused silica prism and recorded by a CCD Camera (Series 2000, Si photodetector, Entwicklungsbüro Stresing). Pump wavelengths at 400 and 267 nm (both 400 nJ per pulse) were generated by second harmonic generation and sum frequency mixing of the 800 and 400 nm pulses. Spot size in the sample was about 200 μm , which was more than twice the white-light spot size. Delay of the pump pulse was managed by a computer controlled translation stage (maximum delay $\sim 1.2 \text{ ns}$, Thorlabs), whereby every second pulse was blocked with an optical chopper (Thorlabs), resulting in spectra with and without excitation. Differentiation results in ΔOD spectra with a time resolution better than 100 fs. Data were collected with an in-house written Labview program.

Supporting Information

Additional information is available on the characterization of [ZrO]₂⁺[F6P]₂⁻ precursor nanoparticles, the C-dot@[ZrO]₂⁺[HPO₄]₂⁻ composite nanoparticles, and the C-dot@[Eu(OH)]₂⁺[HPO₄]₂⁻ composite nanoparticles.

Acknowledgements

K.S. and C.F. are grateful to the Deutsche Forschungsgemeinschaft (DFG) for funding of personnel in the project “Carbon Nanoparticles (C-Dots)” (FE911/8) and TEM equipment (INST 121384/33-1 FUGG). Furthermore, we thank the DFG Graduate School 2039/2 and KIT for continuous support. Open access funding enabled and organized by Projekt DEAL.

Conflict of Interest

The authors declare no conflict of interest.

Keywords: Carbon dots · Fructose · Aqueous synthesis · Phosphate matrix · Fluorescence

- [1] a) V. Georgakilas, J. A. Perman, J. Tucek, R. Zboril, *Chem. Rev.* **2015**, *115*, 4744–4822; b) U. N. Maiti, W. J. Lee, J. M. Lee, Y. Oh, J. Y. Kim, J. E. Kim, J. Shim, T. H. Han, S. O. Kim, *Adv. Mater.* **2014**, *26*, 40–67.
- [2] X. Xu, R. Ray, Y. Gu, H. J. Ploehn, L. Gearheart, K. Raker, W. A. Scrivens, *J. Am. Chem. Soc.* **2004**, *126*, 12736–12737.
- [3] X. T. Zheng, A. Ananthanarayanan, K. Q. Luo, P. Chen, *Small* **2015**, *11*, 1620–1636.
- [4] a) F. Yuan, S. Li, Z. Fan, X. Meng, L. Fan, S. Yang, *Nano Today* **2016**, *11*, 565–586; b) S. Y. Lim, W. Shen, Z. Gao, *Chem. Soc. Rev.* **2015**, *44*, 362–381.
- [5] M. L. Liu, B. B. Chen, C. M. Li, C. Z. Huang, *Green Chem.* **2019**, *21*, 449–471.
- [6] a) K. A. S. Fernando, S. Sahu, Y. Liu, W. K. Lewis, E. A. Gulians, A. Jafariyan, P. Wang, C. E. Bunker, Y. P. Sun, *ACS Appl. Mater. Interfaces* **2015**, *7*, 8363–8376; b) K. Hola, Y. Zhang, Y. Wang, E. P. Giannelis, R. Zboril, A. L. Rogach, *Nano Today* **2014**, *9*, 590–603; c) H. Sun, L. Wu, W. Wei, X. Qu, *Mater. Today* **2013**, *16*, 433–442.
- [7] a) D. I. Abu Rabe, O. O. Mohammed, X. Dong, A. K. Patel, C. M. Overton, Y. Tang, S. Kathariou, Y. P. Sun, L. Yang, *Mater. Adv.* **2020**, *1*, 321–325; b) L. Li, T. Dong, *J. Mater. Chem. C* **2019**, *7*, 3105; c) S. Qu, D. Zhou, D. Li, W. Ji, P. Jing, D. Han, L. Liu, H. Zeng, D. Shen, *Adv. Mater.* **2016**, *28*, 3516–3521; d) A. B. Bourlinos, A. Stassinopoulos, D. Anglos, R. Zboril, M. Karakassides, E. P. Giannelis, *Small* **2008**, *4*, 455–458.
- [8] a) S. Y. Lim, W. Shen, Z. Gao, *Chem. Soc. Rev.* **2015**, *44*, 362–381; b) Y. Wang, A. Hu, *J. Mater. Chem. C* **2014**, *2*, 6921–6939.
- [9] S. N. Baker, G. A. Baker, *Angew. Chem. Int. Ed.* **2010**, *49*, 6726–6744; *Angew. Chem.* **2010**, *122*, 6876–6896.
- [10] a) Q. Tang, W. Zhu, B. He, P. Yang, *ACS Nano* **2017**, *11*, 1540–1547; b) X. Teng, C. Ma, C. Ge, M. Yan, J. Yang, Y. Zhang, P. C. Morais, H. Bi, *J. Mater. Chem. B* **2014**, *2*, 4631–4639; c) S. Chandra, P. Das, S. Bag, D. Laha, P. Pramanik, *Nanoscale* **2011**, *3*, 1533–1540; d) Z.-C. Wang, M. Wang, A. M. Yong, S. Y. Wong, X.-H. Zhang, H. Tan, A. Y. Chang, X. Li, J. Wang, *Chem. Commun.* **2011**, *47*, 11615–11617.
- [11] a) Z. Zhang, W. Sun, P. Wu, *ACS Sustainable Chem. Eng.* **2015**, *3*, 1412–1418; b) S. Sahu, B. Behera, T. K. Maiti, S. Mohapatra, *Chem. Commun.* **2012**, *48*, 8835–8837; c) L. Zhu, Y. Yin, C. F. Wang, S. Chen, *J. Mater. Chem. C* **2013**, *1*, 4925–4932.
- [12] a) Y. Hu, J. Yang, J. Tian, L. Jia, J. S. Yu, *Carbon* **2014**, *77*, 775–782; b) Y. Liu, C. Liu, Z. Zhang, *J. Mater. Chem. C* **2013**, *1*, 4902–4907; c) H. Peng, J. Travas-Sejdic, *Chem. Mater.* **2009**, *21*, 5563–5565.
- [13] a) H. Dong, A. Kuzmanoski, D. M. Göbl, R. Popescu, D. Gerthsen, C. Feldmann, *Chem. Commun.* **2014**, *50*, 7503–7506; b) A. Jaiswal, S. S. Gosh, A. Chattopadhyaya, *Chem. Commun.* **2012**, *48*, 407–409.
- [14] a) X. Wang, K. Qu, B. Xu, J. Ren, X. Qu, *J. Mater. Chem.* **2011**, *21*, 2445–2450; b) H. Zhu, Y. Wang, Y. Li, Z. Wang, F. Yang, X. Yang, *Chem. Commun.* **2009**, *34*, 5118–5120.
- [15] a) H. Zhang, B. Wang, X. Yu, J. Li, J. Shang, J. Yu, *Angew. Chem. Int. Ed.* **2020**, *59*, 19390–19402; *Angew. Chem.* **2020**, *132*, 19558–19570; b) Y. Wang, Y. Li, Y. Yan, J. Xu, B. Guan, Q. Wang, J. Li, J. Yu, *Chem. Commun.* **2013**, *49*, 9006–9008; c) J. Li, B. Wang, H. Zhang, J. Yu, J. Yu, *Small* **2019**, *15*, e1805504.
- [16] a) B. L. Neumeier, M. Khorenko, F. Alves, O. Goldmann, J. Napp, U. Schepers, H. M. Reichardt, C. Feldmann, *ChemNanoMat* **2019**, *5*, 24–45; b) M. Poß, E. Zittel, C. Seidl, A. Meschkov, L. Muñoz, U. Schepers, C. Feldmann, *Adv. Funct. Mater.* **2018**, *28*, 1801074.
- [17] J. G. Heck, J. Napp, S. Simonato, T. Möllmer, M. Lange, H. R. Reichardt, R. Staudt, F. Alves, C. Feldmann, *J. Am. Chem. Soc.* **2015**, *137*, 7329–7336.
- [18] J. Napp, M. A. Markus, J. G. Heck, C. Dullin, W. Möbius, D. Gorpas, C. Feldmann, F. Alves, *Theranostics* **2018**, *8*, 6367–6368.
- [19] J. G. Heck, K. Rox, H. Lünsdorf, T. Lückerrath, N. Klaassen, E. Medina, O. Goldmann, C. Feldmann, *ACS Omega* **2018**, *3*, 8589–8594.
- [20] M. Poß, R. J. Tower, J. Napp, L. C. Appold, T. Lammers, F. Alves, C.-C. Glüer, S. Boretius, C. Feldmann, *Chem. Mater.* **2017**, *29*, 3547–3554.
- [21] V. K. LaMer, R. H. J. Dinegar, *J. Am. Chem. Soc.* **1950**, *72*, 4847–4854.

- [22] S. Abbas, I. Yadav, S. Kumar, V. K. Aswal, J. Kohlbrecher, *Chem. Phys. Lett.* **2017**, *675*, 124–130.
- [23] M. Hurttta, I. Pitkanen, J. Knuutinen, *Carbohydr. Res.* **2004**, *339*, 2267–2227.
- [24] Y. Dong, H. Pang, H. B. Yang, C. Guo, J. Shao, Y. Chie, C. M. Li, T. Yu, *Angew. Chem. Int. Ed.* **2013**, *52*, 7800–7804; *Angew. Chem.* **2013**, *125*, 7954–7958.
- [25] R. Weissleder, *Nature Biotechnol.* **2001**, *19*, 316–317.
- [26] G. Blasse, C. Grabmeier, *Luminescent Materials*, Springer, Berlin 1994.
- [27] J. A. Dodd, S. J. Lipson, W. A. M. Blumberg, *J. Chem. Phys.* **1991**, *95*, 5752–5762.
- [28] C. Schweigert, O. Babii, S. Afonin, T. Schober, J. Leier, N. C. Michenfelder, I. V. Komarov, A. S. Ulrich, A. N. Unterreiner, *ChemPhotoChem* **2019**, *3*, 403–410.

Manuscript received: March 21, 2021
 Revised manuscript received: May 19, 2021
 Accepted manuscript online: May 20, 2021
 Version of record online: June 10, 2021